DTU Library

Mapping of individual dislocations with dark field x-ray microscopy

Jakobsen, Anders Clemen; Simons, Hugh; Ludwig, W. ; Yildirim, C. ; Leemreize, Hanna; Porz, L. ; Detlefs, C. ; Poulsen, Henning Friis

Published in:
Journal of Applied Crystallography

Link to article, DOI:
10.1107/S1600576718017302

Publication date:
2019

Document Version
Early version, also known as pre-print

Journal of Applied Crystallography

ISSN 0021-8898

Mapping of individual dislocations with dark field x-ray microscopy

A. C. Jakobsen,[a] H. Simons,[a] W. Ludwig,[b] C. Yildirim,[b,c] H. Leemreize,[a,d] L. Porz,[e] C. Detlefs[b] and H. F. Poulsen [a]*

[a]Department of Physics, Technical University of Denmark, 2800 Kgs. Lyngby, Denmark, [b]European Synchrotron Radiation Facility, 71 avenue des Martyrs, CS40220, 38043 Grenoble Cedex 9, France, [c]OCAS, J.F. Kennedylaan 3, 9060 Zelzate, Belgium, [d]Danish Technological Institute, Kongsvang Alle 29, 8000 Aarhus Denmark, and [e]Materialwissenschaft, TU Darmstadt, Alarich-Weiss-Strasse 2, 64287 Darmstadt, Germany. Correspondence e-mail: hfpo@fysik.dtu.dk

We present an x-ray microscopy approach for mapping deeply embedded dislocations in three dimensions using a monochromatic beam with a low divergence. Magnified images are acquired by inserting an x-ray objective lens in the diffracted beam. The strain fields close to the core of dislocations give rise to scattering at angles where weak beam conditions are obtained. We derive analytical expressions for the image contrast. While the use of the objective implies an integration over two directions in reciprocal space, scanning an aperture in the back focal plane of the microscope allows a reciprocal space resolution of $\Delta Q/Q < 5 \cdot 10^{-5}$ in all directions, ultimately enabling high precision mapping of lattice strain and tilt. We demonstrate the approach on three types of samples: a multi-scale study of a large diamond crystal in transmission, magnified section topography on a 140μm thick $SrTiO_3$ sample and a reflection study of misfit dislocations in a 120 nm thick $BiFeO_3$ film epitaxially grown on a thick substrate. With optimal contrast, the full width of half maximum of the dislocations lines are 200 nm, corresponding to the instrumental resolution of the microscope.

1. Introduction

Dislocations are typically studied by transmission electron microscopy, TEM. With atomic resolution comprehensive information can be gathered of e.g. the strain field in a dislocation core (Dong & Zhao, 2010), or the 3D arrangement of dislocations in networks (Barnard *et al.*, 2006), (Ramar *et al.*, 2010), (Liu *et al.*, 2014). However, TEM is inherently limited to the study of thin foils. For non-destructive mapping of individual dislocations in the bulk X-ray imaging is prevalent.

In conventional x-ray topography, a 2D detector or film is placed in the Bragg diffracted beam downstream of the sample (Tanner, 1976). The diffracted intensity is projected onto a two-dimensional image, a 'topograph'. This technique allows one to visualize long-range strain fields induced by the dislocations. Three-dimensional mapping can be provided in several ways. First results were achieved by preparing 'stereo pair' diffraction topographs (Lang, 1959), (Haruta, 1965), which provide two views of the defects, followed by recording a number of closely spaced 'section' topographs (Medrano *et al.*, 1997) (Ohler *et al.*, 2000). Synchrotrons made more elaborate methods accessible. In topo-tomography as presented by Ludwig *et al.* (2001), a large number of projections are obtained by rotating the sample about the scattering vector. By generalizing cone beam x-ray tomography, these can be reconstructed into a voxelated 3D model. Topo-tomography has been used to map networks containing hundreds of dislocations. The spatial resolution, however, is inherently limited (see also Tanner (1976)), and was 10 micrometers in the study reported (Ludwig *et al.*, 2001). In a similar manner, laminography has been successfully applied to studies of dislocations in wafers (Hänscke *et al.*, 2012). The limitation on resolution was overcome in a study with a polychromatic nano-beam by Hofmann *et al.* (2013), where all 9 strain components were mapped around one single dislocation with a resolution of 500 nm. The drawback in this case is that the method involves scanning the nano-beam with respect to the sample, a procedure that is relatively slow; hence generalization to mapping an extended network in 3D is not trivial. Recently, studies of dislocations within isolated nano-sized crystals have also been made by x-ray coherent techniques, e.g. Ulvestad *et al.* (2017), but again generalization to bulk samples is not straightforward.

Here we demonstrate a new approach to the three-dimensional characterization of defects within extended internal volumes of near-perfect single crystals, grains or domains. This is based on dark field x-ray microscopy, where an x-ray objective lens is placed in the diffracted beam (Simons *et al.*, 2015; Simons *et al.*, 2018*a*), providing an inverted and magnified projection image on a detector in the imaging plane. The spatial resolution and field-of-view is a function of the magnification, which depends on the lens configuration and the sample-to-objective and objective-to-detector distances. Similar to optical microscopy or TEM, the microscope is also associated with a Fourier/diffraction plane, the back focal plane. A detailed description of the optical properties in the image plane and back focal plane are given in Poulsen *et al.* (2017) and Poulsen *et al.* (2018), respectively.

In the following, we first summarise the acquisition geometry of dark field microscopy. Next we present two methods for mapping dislocations. The former is a magnified version of classical topography. In the latter, an aperture is introduced in the back focal plane to define a certain range in reciprocal space. By scanning the aperture one can visualise the strain field around a dislocation, e.g. with the aim of identifying Burgers vectors. We describe the optical principles and demonstrate the use of the methods by three examples. The first is a full field transmission study of dislocations within the interior of a 400 μm thick synthetic diamond crystal, the second a magnified section topography study of a deformed $SrTiO_3$ sample and the third a full field reflection study of a 120 nm $BiFeO_3$ thin film.

2. The dark field x-ray microscopy set-up

Dark-field x-ray microscopy (Simons *et al.*, 2015) is conceptually similar to dark-field transmission electron microscopy. The experimental geometry and operational principle are shown in Fig. 1: monochromatic x-rays with wavelength λ illuminate the diffracting object. The sample goniometer comprises a base tilt, μ, an ω rotation stage and two orthogonal tilts, χ and ϕ. The sample is oriented such that the Bragg condition is fulfilled, as defined by scattering vector $\vec{Q}$, scattering angle 2θ and azimuthal angle η. An x-ray objective produces an inverted and magnified image in the detector/image plane. Furthermore it acts as a band-pass filter in reciprocal space, which is crucial for polycrystalline specimens as spot overlap can be avoided in this way.

The method development has been motivated primarily by studies of polycrystalline samples. However, grains typically have to be aligned and studied one by one. For simplicity in this article we shall assume the sample to be a single crystal. Furthermore, following current practice the objective will be a compound refractive lens, CRL, (Snigirev *et al.*, 1996) with N identical parabolic shaped lenses with a radius-of-curvature R and a distance between lenslet centres of T.

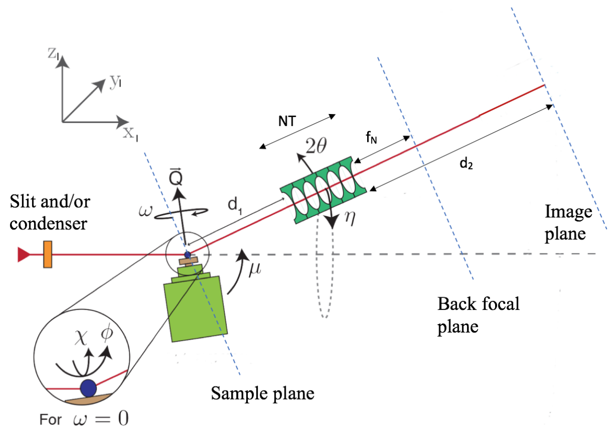

Figure 1
Geometry of dark-field x-ray microscopy. The optical axis of the diffracted beam is defined by the centre of rotation of the sample goniometer, the centre of the objective and the point of normal incidence of the beam on the detector. $\vec{Q}$ is the scattering vector, 2θ the scattering angle, μ, χ and ϕ are tilts, while ω is a rotation around $\vec{Q}$. d_1 is the distance from sample to entry point of the objective, d_2 the distance from the exit point of the objective to the detector and f_N the focal length of the objective. The laboratory coordinate system (x_l, y_l, z_l) is shown.

3D mapping can be obtained in two ways. Firstly, by using a line beam to illuminate slices of the sample one at the time, and subsequently stacking the 2D reconstructions. For some purposes this may be considered a magnified type of section topography, but the use of an x-ray objective implies a separation of angular and spatial degrees of freedom and as such adds additional advantages beyond the geometric magnification. Secondly, similar to the topo-tomography approach mentioned above, by using a full field illumination and recording projections from different viewing angles while rotating the sample about the scattering vector and subsequently using tomography type algorithms to reconstruct the 3D volume.

In Poulsen *et al.* (2017) a comprehensive description of optical properties of the image plan is provided, including expressions for the numerical aperture, NA, the focal length, f_N, the relation between magnification $\mathcal{M}$, working distance d_1 and the distance between lens exit and detector plane d_2 as well as the field-of-view, direct space resolution and reciprocal space resolution. It is shown how the local variation in tilt of the scattering vector (i.e. the local pole figure or mosaic spread) can be mapped by stepping the sample through two orthogonal tilts. The first is either the base tilt, μ, or an equivalent rotation around y_l by a combination of tilts χ and ϕ — in both cases representing the 'rocking' of the sample in classical topography. The second is an orthogonal tilt, enabled by another combination of χ and ϕ. This represents the 'rolling' of the scattering vector. The axial strain can be measured by a longitudinal $(\theta - 2\theta)$ scan, where 2θ is varied by a combined translation and rotation of the objective and the detector.

Similar to classical light microscopy, the hard X-ray microscope is associated with a 'Fourier plane', placed at a distance of f_N from the exit of the CRL, cf. Fig. 1. The intensity distribution in this back focal plane (BFP) is equivalent to the distribution in the Fraunhofer far field limit. Poulsen *et al.* (2018) presents a complementary description for the optics properties of the BFP. Here an alternative approach to mapping the local tilt and local axial strain is provided under the heading of local reciprocal space mapping. By inserting an aperture in the BFP, the images acquired in the image plane will represent the direct space image corresponding to a certain (small) region in reciprocal space selected by this aperture. By translating the aperture within the BFP, the center position of the region can be varied. Similar to the operation of a TEM (Williams & Carter, 2009) the possibility to combine local information in direct and reciprocal space is seen as a major asset of dark field x-ray microscopy.

In the following we shall explore the microscope for mapping the axial and two off-diagonal strains around individual dislocations, corresponding to small variations in ϕ, χ and 2θ. We will primarily be concerned with the contrast and resolution within a single image: algorithms for the generalisation to 3D mapping will be presented elsewhere.

3. Methodology

3.1. Weak beam contrast mechanism

In this paper we shall assume that the scattering vector probed is in the proximity of a reciprocal lattice vector, $\vec{Q}_0$. We will neglect effects due to (partial) coherence and assume that dynamical effects only takes place within a sphere in reciprocal space around the lattice point, $\vec{Q}_0$, with radius r_{dyn}. By definition, when probing parts of reciprocal space with $\left|\vec{Q}-\vec{Q}_0\right| > r_{dyn}$ kinematical scattering applies. We shall use the phrase 'weak beam contrast'.

We shall not be concerned with the symmetry of the unit cell, and reciprocal space and strain tensors both refer to a simple cubic system. Including crystallography is straightforward in principle, but the more elaborate equations makes the treatment less transparent. Moreover, we will consider only the case of a synchrotron beam with an energy band $\Delta E/E$ of order 10^{-4} or less. Unless focusing optics are used the incoming beam will have a divergence of $\Delta\zeta \approx 0.1$ mrad or smaller. In comparison the numerical aperture of the objective is much larger: $NA \approx 1$ mrad.

In the following we estimate the width of the intensity profile from a single straight dislocation within this weak beam contrast model. This estimate will be used for a simple comparison with experimental data and for discussing current and future use. For reasons of simplicity we consider a fully illuminated straight screw dislocation with Burgers vector $\vec{B}$ aligned with $\vec{Q}_0$ and parallel to the z-axis at $x = y = 0$. In this case, when rotating around $\vec{Q}_0$ the strain field and projections are invariant. In a classical dislocation model the non-zero strain components are

$$e_{zx} = -\frac{B}{2\pi}\frac{y}{x^2+y^2}; \qquad e_{zy} = \frac{B}{2\pi}\frac{x}{x^2+y^2}. \tag{1}$$

In general the strain components e_{ij} associated with an isolated dislocation falls off as $e_{ij} \approx \frac{B}{2\pi}\frac{1}{r}$, where r is the radial distance from the core of the dislocation.

It is natural to introduce a reciprocal space coordinate system $(\hat{q}_{\mathrm{rock}}, \hat{q}_{\mathrm{roll}}, \hat{q}_{\|})$ with $\hat{q}_{\|}$ parallel to $\vec{Q}_0$ and $\hat{q}_{\mathrm{roll}}$ parallel to the rolling direction and perpendicular to the vertical scattering plane. For the simple cubic system and the case introduced above of a screw dislocation aligned with $\vec{Q}_0$ and $\omega = 0$ we have $\Delta Q_{\mathrm{rock}}/\left|Q_0\right| = -e_{zx}$, $\Delta Q_{\mathrm{roll}}/\left|Q_0\right| = -e_{zy}$ and $\Delta Q_{\|}/\left|Q_0\right| = -e_{zz}$.

3.2. Mapping dislocations by magnified topography

As usual for imaging systems we will define the sample plane as a plane perpendicular to the optical axis, cf. Fig. 1. Let this be spanned by $(\hat{y}_s, \hat{z}_s)$. It is natural to have another parameterisation of reciprocal space which is co-linear to this plane. For $\omega = 0$ we define this by coordinates $(\hat{q}_{\mathrm{rock}'}, \hat{q}_{\mathrm{roll}}, \hat{q}_{2\theta})$, with $\hat{q}_{\mathrm{rock}'}$ parallel to the optical axis.

It is shown in Poulsen *et al.* (2017) that in this coordinate system the resolution function is a Gaussian with principal axis aligned with the coordinate axes and with widths (FWHM)

$$\Delta Q_{\mathrm{rock}'} = \frac{|Q_0|}{2\cos(\theta)}\Delta\zeta, \tag{2}$$

$$\Delta Q_{\mathrm{roll}} = \frac{|Q_0|}{2\sin(\theta)}NA, \tag{3}$$

$$\Delta Q_{2\theta} = \frac{|Q_0|}{2\tan(\theta)}NA. \tag{4}$$

This shows that $\Delta Q_{\mathrm{rock}'} \ll \Delta Q_{\mathrm{roll}} \approx \Delta Q_{2\theta}$ and the resolution function is in fact an oblate spheroid.

Comparing Eq. 1 to Eqs. 3 and 4, it appears that for experimentally relevant values of r, **the intensities on the detector are the result of a 2D projection in reciprocal space**: the objective's NA effectively integrates over directions $\hat{q}_{2\theta}$ and $\hat{q}_{\mathrm{roll}}$. In addition, the intensities are 1D projections in direct space, along the axis of the diffracted beam.

The resolution in the 'rocking direction' is in fact a convolution of the Darwin width of the sample and the divergence of the incoming beam. For simplicity, in Eq. 2 and throughout this manuscript we shall neglect the Darwin width.

Next, let us consider the model system of section 3.1. For $\omega = 0$ we integrate over e_{zy}. The intensity distribution is then a function of only two variables $I = I(y, e_{zx})$. We can determine the path length along x for a given y and strain interval $\mathrm{d}e_{zx}$ by inverting Eq. 1 and differentiating $\mathrm{d}x/\mathrm{d}e_{zx}$, see Appendix. As a result

$$I(y, e_{zx}) \propto \int_{-\infty}^{\infty} f(y-y') \left| \int_{u_1}^{u_2} \frac{g(e_{zx}-u)}{u^2\sqrt{-\frac{B}{2\pi u y'}-1}}\mathrm{d}u \right| \mathrm{d}y'; \tag{5}$$

with

$$u_1 = -\frac{B}{2\pi y'}; \qquad u_2 = -\frac{By'}{2\pi(y'^2+(T_c/2)^2)} \tag{6}$$

Here $f(y)$ is the point spread function and $g(e_{zx})$ is the resolution in e_{zx}. In the following we shall assume both to be Gaussian distributions. T_c is the thickness of the crystal in the direction of the diffracted beam. $||$ symbolises the absolute value.

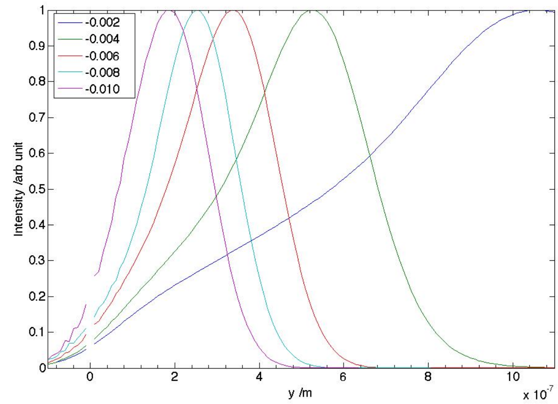

Figure 2
Simulated intensity profile perpendicular to a screw dislocation with the offset in rocking angle in degrees as parameter. All curves are normalized to 1. See text.

Simulations of the intensity profile across a screw dislocation are shown in Fig. 2 using parameters relevant to the experiments presented later, including a point spread function $f(y)$ with a FWHM of 180 nm, a strain resolution function $g(e_{zx})$ with a FWHM of 0.02 mrad and a sample thickness of 400 μm. With increasing offset in rocking angle the width of the curves asymptotically approaches the spatial resolution, while the peak position in direct space, r, and strain (angular offset) approximately follows $e = \frac{B}{2\pi r}$.

For applications, a main challenge of any topography method is overlap of signal from dislocation lines. This effectively limits the approach in terms of dislocation density. It appears that in the weak beam contrast description the likelihood of overlap is determined by how far off the peak on the rocking curve one can go while still maintaining a contrast. The profiles shown in Fig. 2 are normalised. If not normalised, the amplitude of the profiles falls off rapidly with offset in rocking angle. Hence, signal-to-noise becomes critical.

Another concern is the nature of the tails of the distributions $f(y)$ and $g(e_{zx})$. If these tails are intense, such as in Lorentzian distributions, the contrast deteriorates. Hence, being able to design and characterise the resolution functions is important. This can be achieved with an aperture in the BFP.

3.3. Mapping dislocations using an aperture in the back focal plane

Dark field imaging is one of the basic modalities of a TEM (Williams & Carter, 2009). By inserting an aperture in the back focal plane, one selects a certain region in reciprocal space and uses the diffracted signal within this region as contrast to image the sample. In Poulsen *et al.* (2018), we introduce the equivalent technique for hard x-ray microscopy. The relation between position (y_B, z_B) in the back focal plane, the angular offset in rocking angle $\phi - \phi_0$ and reciprocal space is

$$q_{\text{rock}} = \frac{\Delta Q_{\text{rock}}}{\left|\vec{Q}_0\right|} = (\phi - \phi_0) - \frac{\cos(N\varphi)}{2\sin(\theta) f_N} z_B \sin(\theta), \quad (7)$$

$$q_{\text{roll}} = \frac{\Delta Q_{\text{roll}}}{\left|\vec{Q}_0\right|} = \frac{\cos(N\varphi)}{2\sin(\theta) f_N} y_B, \quad (8)$$

$$q_{\|} = \frac{\Delta Q_{\|}}{\left|\vec{Q}_0\right|} = \frac{\cos(N\varphi)}{2\sin(\theta) f_N} z_B \cos(\theta), \quad (9)$$

with $\varphi = \sqrt{T/f}$ being a measure of the ‘refractive power’ of the lens, and f_N being the focal length. The last term in Eq. 7 and the $\cos(\theta)$ factor in Eq. 9 originates in the fact that rocking the sample is a movement in a direction which is at an angle of θ with the optical axis (the direction of the diffracted beam).

Unfortunately, if the aperture gap D is smaller than or comparable to the diffraction limit λ/NA, the spatial resolution in the imaging plane will deteriorate. On the other hand, using wavefront propagation in Poulsen *et al.* (2018) we demonstrated that the aperture will not influence the spatial resolution if the gap is sufficiently large. For a specific application introduced below the minimum gap is 80 μm. In order to provide a high resolution both in reciprocal space and in direct space, we therefore propose to move a square aperture with a sufficiently large gap in a regular 2D grid within the BFP and to regain reciprocal space resolution by a deconvolution procedure as follows: let the positions of the center of the slit be $(y_B, z_B) = D/M \cdot (m, n)$, with $m = -M, -M+1, \ldots, M$ and $n = -M, -M+1, \ldots M$. For fixed rocking angle ϕ and for a given pixel on the detector, let the set of intensities measured in this detector pixel be $S_{m,n}$.

Now, consider the intensities $I_{m,n}$ for an aperture of size D/M, in the hypothetical case that the diffraction limit can be neglected. Moreover, assume the diffracting object is bounded such that there is no diffracted intensity outside the grid. Then, in the first quadrant we have: for $-M < m \leq 0$ and $-M < n \leq 0$

$$I_{m,n} = S_{m,n} - S_{m,n-1} - S_{m-1,n} + S_{m-1,n-1}. \quad (10)$$

For the other quadrants similar expressions can be established. Hence, using this simple difference equation we can generate high resolution q maps.

In Poulsen *et al.* (2018) it is also found that the FWHM of the resolution function in the BFP can be $\Delta Q / \left|\vec{Q}_0\right| = 4 \cdot 10^{-5}$ or better in all directions, which is substantially smaller than the angular range of the diffracted beam. We conclude that by placing an aperture in the back focal plane we can generate a 5D data set. Hence, **we can associate each detector point with a reciprocal space map**. Then the only remaining integration is in the thickness direction in real space. We anticipate this enhanced contrast to be useful for identifying Burgers vectors and for improved forward models. In particular this may enable studies of samples with higher dislocation densities as one can separate dislocations that are overlapping in the greyscale images.

A significant simplification arises if we use the formalism of elasticity theory. Then each point (x_s, y_s, z_s) in the sample is associated with one point in reciprocal space corresponding to the three strain components: (e_{zx}, e_{zy}, e_{zz}). Let the recorded intensities be $I(\vec{q}, y_d, z_d)$ with (y_d, z_d) being the detector coordinates, $\vec{q} = (q_{\text{rock}}, q_{\text{roll}}, q_{||})$ and strain vector $\vec{e} = (e_{zx}, e_{zy}, e_{zz})$. Then for $\omega = 0$ we have

$$I(\vec{q}, y_d, z_d) \propto \iiint \mathrm{d}x_s\, \mathrm{d}u\, \mathrm{d}v\, f(y_d - u, z_d - v) \tag{11}$$

$$\int \mathrm{d}^3\vec{q}'\, g(\vec{e}(x_s, u/\mathcal{M}, v/\mathcal{M}) - \vec{q}'). \tag{12}$$

Here $\mathcal{M}$ is the magnification in the x-ray lens, f is the detector point-spread-function and g is the reciprocal space resolution function.With the square aperture in the BFP, the function g is a box function in two directions.

With respect to implementation, it may also be possible to transfer additional TEM modalities. In particular, *annular dark-field imaging* is a candidate for fast 3D mapping of dislocations. Blocking the central beam ay be an elegant way to remove spurious effects due to dynamical diffraction.

4. Experimental demonstrations

To illustrate the potential and challenges of our approach, we report on the results from three different type of use. Three samples were studied at beamline ID06 at the ESRF over two beamtimes and under slightly different configurations (as the beamline instrumentation evolved during this period).

In all cases, a Si (111) double monochromator was used to generate a beam with an energy bandwidth of $\sigma_e = 0.6 \cdot 10^{-4}$ (rms). The goniometer with all relevant degrees of freedom, cf. Fig 1, is placed 58 m from the source. Pre-condensing is performed with a transfocator (Vaughan *et al.*, 2011) positioned at a distance of 38.7 m from the source. For section topography, a 1D condenser was used to define a horizontal line beam. Otherwise, a slit defined the dimensions of the beam impinging on the sample. Two detectors were in use, firstly a nearfield camera, placed close to the sample, which may provide classical topographs and topo-tomograms without the magnification by the x-ray objective. Secondly, a farfield camera placed at a distance of ≈ 5.9 m for imaging the magnified beam in the image plane of the microscope. Both detectors were FRELON 2k x 2k CCD cameras, which are coupled by microscope optics to a LAG scintillator screen. The objective comprised N identical parabolically shaped Be lenses with a radius of curvature $R = 50\,\mu$m and thickness T. A square slit with adjustable gaps and offsets was placed in the BFP. The surface normals of all detectors and slits were aligned to be parallel to the optical axis. The nearfield camera and the aperture in the BFP could be translated in and out of the diffracted beam.

4.1. Transmission experiment

The sample was an artificially grown diamond plate, type IIa, with a thickness of 400μm, see Burns *et al.* (2009). It was mounted in a transmission Laue geometry. The 17 keV incident beam had a divergence (FWHM) of 0.04 mrad, and dimensions of 0.3 mm $\times$ 0.3 mm. With $N = 72$ and $T = 2$ mm, the focal length of the objective was $f_N = 0.245$ m. The effective pixel size of the near and far-field detector was 0.62 μm and 1.4 μm, respectively. The magnification by the x-ray objective was measured to be $\mathcal{M} = 16.2$, implying a numerical aperture of $NA = 0.643$ mrad and an effective pixel size of 93 nm. The detector was then binned 2 $\times$ 2. Using Eqs. 2 – 4 the FWHMs of the reciprocal space resolution function in the three principal directions become $(\Delta q'_{\text{rock}}, \Delta q_{\text{roll}}, \Delta q_{2\theta}) = (0.000062\text{Å}^{-1}, 0.0055\text{Å}^{-1}, 0.0055\text{Å}^{-1})$.

An in-plane $\{111\}$ reflection was used for the study. The length of the diffraction vector and Burgers vector are $\left|\vec{Q}_0\right| = 3.051\,\text{Å}^{-1}$ and $\left|\vec{B}\right| = 2.522\,\text{Å}$, respectively. Using the formalism of Als-Nielsen & McMorrow (2011), the corresponding Pendellösung length, and Darwin width are $\Lambda_g = 35\,\mu$m and $w_g^\theta = 0.0119$ mrad (FWHM), respectively. Hence, the incoming beam divergence dominates the Darwin width. The data set involved 36 ω projections over a range of 360 degrees. For each projection images were acquired in a 31 $\times$ 31 grid in rocking angle μ (with steps of 0.0016 deg) and 2θ (steps of 0.0032 deg). Exposure times were 1 second.

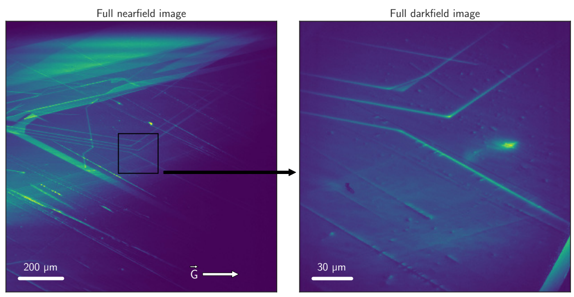

Figure 3
Projection images of a large single crystal diamond in the transmission experiment. Nearfield detector image with no x-ray objective and corresponding dark field image acquired with the diffraction microscope, both for $\mu - \mu_0 = 0.002$ deg. The magnification of the microscope is $\mathcal{M} = 16.2$, The direction of the rotation axis is marked by an arrow.

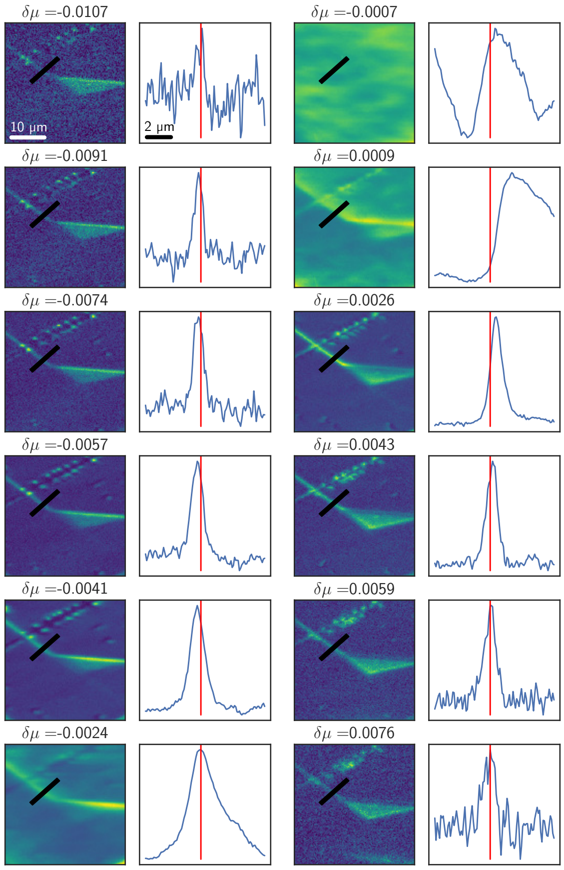

Figure 4
Zoom of data from the transmission experiment, in each image showing one screw dislocation (left) attached to a triangular area associated with a stacking fault. The variation with rocking angle $\delta\mu$ is shown. The lineplots represent the integrated intensity as function of distance perpendicular to the dislocation line, as marked by the 5 pixel thick black lines. The lineplots are normalized to max intensity. The red lines indicate the interpolated position of the dislocation line.

Fig. 3 shows an image from the nearfield detector and the corresponding dark field image from the diffraction microscope. The latter is inverted for ease of comparison. The difference in field-of-view, FOV, is evident, as is the fact that the objective magnifies the image without visible distortions.

Fig. 4 shows the diffracted signal as a function of rocking angle from a specific location in microscope image. It appears that the signal is corrupted by dynamical diffraction effects until at least $\delta\mu = \pm 0.002°$. The signal to noise ratio allows useful observations out to $\delta\mu \approx \pm 0.008°$, corresponding to a transverse strain of $\pm 1.4 \cdot 10^{-4}$. Similar plots of the intensity profile in the the radial direction (obtained by a simultaneous translation in μ and 2θ by $\delta\mu = \frac{1}{2}\Delta 2\theta$) — also known as the 'longitudinal direction' — showed a very similar sensitivity. Hence, both 'rocking' and 'longitudinal' contrast are validated. As expected no contrast was detectable in the rolling and 2θ directions, due to the convolution of the diffracted signal with the numerical aperture of the objective.

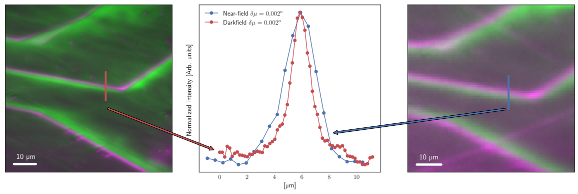

Figure 5
Diffraction images from the same region acquired with the diffraction microscope (left) and the nearfield camera (right). In both cases two images are overlaid: a purple one and a green one representing offsets of the rocking angle μ by $+0.002°$ and $-0.002°$, respectively. Shown in the middle are line plots of the green images representing the intensity distribution perpendicular to the dislocation line.

In Fig. 5 left two diffraction images are overlaid, corresponding to left and right of the Bragg peak on the rocking curve. As anticipated the signal is antisymmetric with respect to the diffraction lines. Line profiles of the intensity across the dislocation lines reveal that a center line between the purple and green curves can be established with high accuracy, 50 nm or better. Comparing to the corresponding signal from the nearfield camera, see Fig. 5 right, the contrast and resolution of the dark field microscopy setup is clearly better. However, the resulting width of the dislocation line is approx. 1.5 μm FWHM. In comparison the simple kinematical model of section 3.1 predicts a width of $\approx$ 200 nm, cf. Fig. 2.

One possible cause for the broadening is field of view. To estimate this effect, we note that a given incoming ray traversing through the strain field a dislocation can be scattered in different directions. When the dislocation is in the sample plane, these diverging rays are all collected in the image plane. If displaced by e.g. 100 μm, geometrical optics expressions in Simons *et al.* (2017) predicts a diffraction limited (real space) resolution with a FWHM of 100 nm for a strain range of $\pm 1.4 \cdot 10^{-4}$. Hence, depth of field cannot be the cause.

The dominant cause of discrepancy is instead considered to be alignment of the microscope, that was problematic at the time due to the *ad hoc* character of the set-up.

4.2. Magnified section topography experiment

Within the weak beam regime one may reduce the likelihood of overlap of dislocations in the images by narrowing the incident beam in the vertical direction (see Fig. 2). By introducing a condenser we can furthermore improve the S/N ratio, at the expense of an increased divergence. In principle, one can adjust the height of the incoming beam to match the spatial resolution. 3D mapping can then be performed layer-by-layer. However, identifying points is more difficult than identifying lines, and 1D condensers providing a micrometer-sized beam tend to be more efficient than those producing a nanometer-sized beam. Hence, it may be optimal to operate with an incoming box beam having a large aspect ratio. We shall use the term 'magnified section topography' for this setting.

In this experiment, the sample was a wedged shaped piece of $SrTiO_3$, where surfaces had been polished mechanically. It was mounted in a transmission Laue geometry, using an in-plane

{110} reflection for the study. The 15.6 keV beam was condensed by a CRL with 55 1D Be lenslets to generate a beam (FWHM) of size $4.2 \times 300\,\mu\text{m}^2$. The objective configuration was in this case $N = 45$, $T = 1.6$ mm, leading to a focal length of $f_N = 0.406$ m. The measured x-ray magnification was 12.32 and consequently the numerical aperture had an rms width of $\sigma_a = 0.24$ mrad. The far-field detector had an effective pixel size of 122 nm. A rocking scan was made over a range of 0.5 deg, with 70 steps and exposure times of 1 second.

Fig. 6 shows a raw image. The top point of the wedge is far to the left of this image. Generally speaking the weak beam scattering signal is confined to two regions, adjacent to the two external boundaries (top and bottom in the figure). We speculate that these have formed during polishing. As shown in the figure, at a certain distance to the top of the wedge, point dislocations are created that bridge the gap between the two surface layers. The intensity profile across one of these vertical lines is shown in Fig. 7. It exhibits a FWHM of 210 nm. In Fig. 6 in the vicinity of the prominent vertical dislocations a network of other dislocations pointing in near random directions are seen. Their linewidths are in some cases below 200 nm, but the statistics is poor. 200 nm is comparable to the spatial resolution of the instrument.

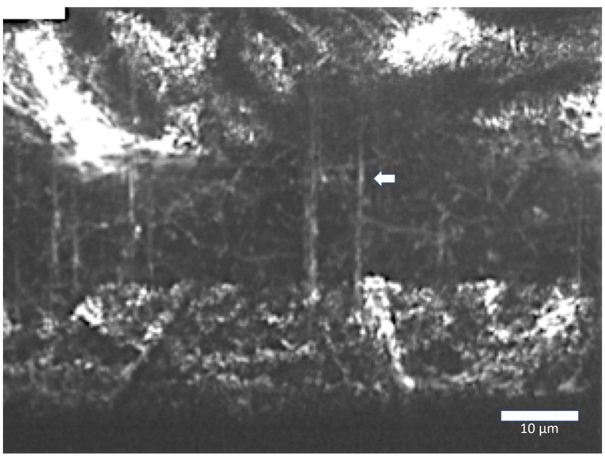

Figure 6
A raw image from the magnified section topography study of a $SrTiO_3$ wedge sample where surfaces near regions (top and bottom) are deformed due to mechanical polishing. The offset in rocking angle is 0.5 mrad. One of the dislocations is marked by an arrow.

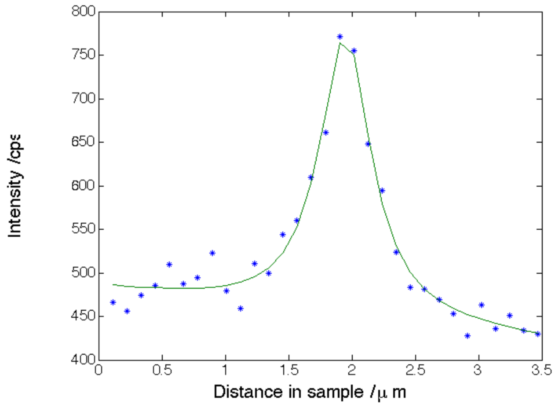

Figure 7
Intensity profile across the dislocation marked by an arrow in Fig. 6 (dots) and corresponding fit to a Lorentzian (line). The fitted FWHM value is 210 nm.

4.3. Reflection experiment

Mapping individual dislocations is of great interest also for films and buried layers. Often these have to be studied in a reflection geometry, as the X-rays cannot penetrate the substrate. The reflection geometry implies a parallax effect in the vertical direction and 3D mapping requires special algorithms, e.g. laminography (Hänscke *et al.*, 2012). To illustrate the potential of hard x-ray microscopy for such samples, we have studied misfit dislocations in $BiFeO_3$ thin films. First results are presented in Simons *et al.* (2018*b*). In short, individual dislocations are identified, and their axial strain field characterized by means of a '$\theta - 2\theta$-scan': a combined translation and rotation of the sample, the objective and the far field detector. Here we report on additional work, where we illustrate the reciprocal space mapping introduced in section 3.3 by means of translating an aperture in the BFP. The ultimate aim for this type of study is to repeat the reciprocal space mapping for a set of ω projection angles in order to reconstruct the strain field for each voxel in the sample. Addressing this challenge is an exercise in vector tomography (Schuster, 2008) and is outside the scope of this paper. Here a simple data analysis is presented for the case of one projection.

The sample was a 120 nm thick film of ⟨001⟩-oriented $BiFeO_3$, grown via pulsed laser deposition on a $SrRuO_3$ electrode layer and ⟨110⟩-oriented $DyScO_3$ single crystalline substrate. This was mounted for a reflection study on the (002) reflection — at $2\theta = 22.6$ deg. In this case the 15.6 keV beam from the transfocator was only moderated by a slit close to the sample. The objective and detector configuration were identical to those of section 4.2. The aperture in the BFP had a square opening of 80 μm. Within the approach of section 3.3 this aperture was translated in a 2D grid with a step size of 30 μm. At each position a rocking scan was made with a step size of 0.001 deg and with exposure times of 2 seconds.

Deconvoluting the signal according to Eq. 10 each point in the sample plane was associated with a reciprocal space map. The voxel size of this map is $\Delta Q/|Q| = (1.7 \cdot 10^{-5}, 1.6 \cdot$

$10^{-4}, 1.6 \cdot 10^{-4})$ in the rock', roll and 2θ directions, respectively.

Zooming in on one dislocation, we illustrate in Fig. 8 the richness of the results obtained. To the left is shown the result with no aperture in the BFP for two offsets in rocking angle. The remainder of the subplots are corresponding results based on the aperture scan. For each point in the detector plane a Gaussian fit was made to the intensity profile arising from scanning the aperture horizontally. Using Eq. 8 this is converted into a relative shift q_{roll}. The fitted center position and width (FWHM) are shown in column 2 and 3, respectively. In columns 4 and 5 are shown the result of an analogous fit to the intensity profile arising from scanning the aperture vertically. Using Eq. 9 this is converted into a relative shift $q_{||}$. All shifts in turn can be directly related to strain components e_{zy} and e_{zz}, while the rocking profile gives access to e_{zx}.

The rocking profiles (not shown) exhibits a clear asymmetry, analogue to that shown in Fig. 4. The second column of Fig. 8 reveals that the rolling profiles have a similar left-right asymmetry. Near the dislocation core the profile has a dip in the center, evident as a large increase in the FWHM of the one-peak fit (third column). In contrast there is no noticeable variation in the longitudinal direction (columns 4 and 5). These findings are consistent with the response from the strain field from a single dislocation with the Burgers vector pointing in the direction of the surface normal, as anticipated for misfit dislocations.

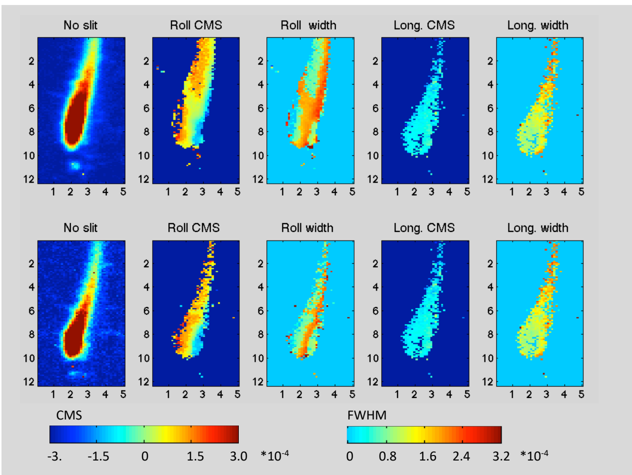

Figure 8
Images of a dislocation in a $BiFeO_3$ film acquired at an offset in rocking angle from the main peak of $\phi = 0.01$ deg (row above) and $\phi = 0.015$ deg (row below) . The contrast is set differently in the two rows. First column: no aperture in the back focal plane; red is maximum intensity, blue is background. Other four columns: results from scanning an aperture of fixed size in the back focal plane. For each pixel on the detector, Gaussian type fits were made to the profile in the rolling and longitudinal directions, respectively. Shown are the center-of-mass positions and the FWHM in units of $\Delta Q/|Q_0|$, as determined by Eqs. 8 and 9. The unit on the axes is μm and refers to the detector plane.

5. Discussion

Dark field microscopy is fundamentally different from classical x-ray topography, as rays emerging in various directions from one point in the sample plane are focused onto a spot in the image plane, rather than leading to a divergent diffracted beam. This implies that the detector can be placed many meters away and that the space around the sample is limited by the objective, not the detector. Moreover, the high spatial resolution allows to visualise the core of the strain field. This simultaneously enables the dislocations to appear as thin lines and scattering to be sufficiently offset from the Bragg peak that weak beam conditions apply. Below we first present the perceived main limitations of the technique and discuss options to overcome these. Next we briefly outline the scientific perspective.

Dynamical diffraction effects. The 'weak beam' condition presented strongly simplifies the data analysis and interpretation. In practice, it is likely that dynamical or coherent effects needs to be considered in some cases. A treatment of dynamical scattering in the context of x-ray topography can be found in e.g. Gronkowski & Harasimowicz (1989) and Gronkowski (1991). However, as mentioned previously, the geometry of data acquisition is fundamentally differently in a microscope. A dynamical treatment of the scattering of a dislocation line in the context of a microscope exists for TEM (Hirsch *et al.*, 1960), but has to the knowledge of the authors yet to be generalized to x-ray microscopy. In a heuristic manner with dark field microscopy we attempt to overcome the issue with dynamical effects in two ways:

- By improving both the spatial and angular resolution it becomes possible to probe parts of reciprocal space which are further from r_{dyn}.
- By combining projection data from a number of viewing angles we anticipate that 'dynamical effects can be integrated out'. Similar strategies have led the electron microscopy community to apply annular dark-field imaging for providing accurate crystallographic data.

Spatial resolution. The spatial resolution sets an upper limit on the density of dislocations that can be resolved. With increasing spatial resolution, one can monitor the strain and orientation fields closer to the core. At the same time, dynamical diffraction effects becomes smaller as one is probing parts of reciprocal space that are further away from the Bragg peak. In practice, the limitation of the technique is currently set by aberrations caused by the lens manufacture and by signal-to-noise considerations. With the possibility of providing a reciprocal space map for each voxel in the sample, cf. section 3.3, overlap of the diffraction signals from dislocation lines can be handled.

To our understanding there is no fundamental physics prohibiting a substantial increase in the spatial resolution of dark field microscope. With ideal CRL optics hard x-ray beams may be focused to spot sizes below 10 nm (Schroer & Lengeler, 2005). Using zone plates as objectives, at x-ray energies below 15 keV, bright field microscopes are in operation with resolutions at 20 nm. For work at higher x-ray energies, there has recently been much progress with multilayer Laue lenses, which seem to promise imaging with superior numerical apertures and much reduced aberations (Morgan *et al.*, 2015). Finally, the next generation of synchrotron sources will be 10 – 100 times more brilliant than the current sources (Eriksson *et al.*, 2014).

This will benefit both spatial resolution (via improved signal-to-noise) and time resolution.

Probing only one diffraction vector. As for any other diffraction technique, the contrast in visualizing the dislocations is proportional to $\vec{Q} \cdot \vec{B}$. Dislocations with a Burgers vector nearly perpendicular to the ω rotation axis are therefore invisible. In order to map all dislocations and/or to determine all components of the strain tensor one has to combine 3D maps acquired on several reflections.

Scientific outlook. The higher resolution in 3D offers new perspectives on dislocation geometry, including measurements of distances and dislocation curvatures (and the balance of line tension by local stresses). This may be relevant for models of dislocation dynamics, and the visualisation of dislocations under e.g. indentations. With respect to dynamical diffraction effects, we remind that extinction lengths for 30 keV x-rays are about 100 times larger than the corresponding extinction lengths for 200 keV electrons. This points to high resolution studies of dislocation dynamics in foils at least 10 μm thick.

Studies of dislocation structures within grains or domains are facilitated by the fact that dark field microscopy is easy to integrate with coarse scale grain mapping techniques such as 3-Dimensional X-ray Diffraction, 3DXRD (Poulsen & Fu, 2003; Poulsen, 2012; Hefferan *et al.*, 2012) and Diffraction Contrast Tomography, DCT (King *et al.*, 2008) (Ludwig *et al.*, 2009).

6. Conclusion

We have demonstrated an x-ray microscopy approach to characterizing individual dislocations in bulk specimens. The method combines high penetration power, a data acquisition time for 3D maps of minutes, and the possibility to study local internal regions by magnifying the images. The spatial resolution is in this proof-of-concept work 200 nm. The limitation is the quality of the focusing optics and the signal-to-noise ratio. With improved x-ray sources and optics this opens the door to studies with a substantially higher spatial resolution. The high resolution allows studies of samples with higher densities of dislocations, and at the same time it enables to probe the material at rocking angles with a large offset from the main peak, where the weak beam condition is fulfilled.

The method can be extended to mapping of the e_{zx}, e_{zy} and e_{zz} fields by scanning a fixed gap aperture in the back focal plane of the objective and by rocking the sample.

We thank Jürgen Härtwig for use of the diamond crystal, Ying-Hao Chu and Nagarajan Valanoor for provision of the $BiFeO_3$ sample and ESRF for beamtime. We are grateful for scientific discussions with Archie Howie, Jürgen Rödel, Jakob Wegener, Wolfgang Pantleon, Jakob Schiøetz, Grethe Winther, Søren Schmidt, Alberto Cereser, Anter El-Azab, Anders Filsoe Petersen, Jeppe Ormstrup and Yubin Zhang. The team acknowledges support from the Danish instrument center Danscatt, and an ERC Advanced Grant 291321 - d-TXM. H.S. acknowledges financial support from a DFF-FTP individual post doc program. H.L. acknowledges financial support for an individual postdoc program from Innovation Fund Denmark, grant 7039-00030B.

References

Als-Nielsen, J. & McMorrow, D. (2011). *Elements of modern X-ray physics*. Wiley.
Barnard, J., Sharp, J., Tong, J. & Midgley, P. (2006). *Phil. Mag.* **86**, 4901–4922.
Burns, R., Chumakov, A., Connell, S., Dube, D., Godfried, H., Hansen, J., Härtwig, J., Hoszowska, J., Masiello, F. & Mkhonza, L. (2009). *Journal of Physics: Condensed Matter*, **21**, 364224.
Dong, Z. & Zhao, C. (2010). *Physica B*, **405**, 171–174.
Eriksson, M., van der Veen, J. & Quitmann, C. (2014). *J. Synchrotron Rad.* **21**, 837–842.
Gronkowski, J. (1991). *J. Physics Reports*, **206**, 1–41.
Gronkowski, J. & Harasimowicz, T. (1989). *Z. Phys. B*, **76**, 345–351.
Hänscke, D., Helfen, L., Altapova, V., Danilewsky, A. & Baumbach, T. (2012). *Appl. Phys. Lett.* **101**, 244103.
Haruta, K. (1965). *J. Appl. Phys.* **36**, 1789–1790.
Hefferan, C., Lind, J., Li, S., Lienert, U., Rollett, A. & Suter, R. (2012). *Acta Mater.* **60**, 4311–4318.
Hirsch, P., Howie, A. & Whelan, M. (1960). *Phil. Trans. R. Soc. A*, **252**, 499.
Hofmann, F., Abbey, B., Liu, W., Xu, R., Usher, B., Balaur, E. & Liu, Y. (2013). *Nature Comm.* **4**, 2774.
King, A., Johnson, G., Engelberg, D., Ludwig, W. & Marrow, J. (2008). *Science*, **321**, 382–385.
Lang, A. (1959). *Acta Cryst.* **12**, 249–250.
Liu, G., House, S., Kacher, J., Tanaka, M., Higashida, K. & Robertson, I. (2014). *Mater. Char.* **87**, 1–11.
Ludwig, W., Cloetens, P., Härtwig, J., Baruchel, J., Hamelin, B. & Bastie, P. (2001). *J. Appl. Cryst.* **34**, 602–607.
Ludwig, W., Reischig, P., King, A., Herbig, M., Lauridsen, E. M., Johnson, G., Marrow, T. J. & Buffiere, J. Y. (2009). *Rev. Sci. Instrum.* **80**, 033905.
Medrano, C., Rejmankova, P., Ohler, M. & Matsouli, I. (1997). *Nuov. Cim. D*, **19**, 195–203.
Morgan, A. J., Prasciolu, M., Andrejczuk, A., Krzywinski, J., Meents, A., Pennicard, D., Graafsma, H., Barty, A., Bean, R. J., Barthelmess, M., Oberthuer, D., Yefanov, O., Aquila, A., Chapman, H. N. & Bajt, S. (2015). *Scientific Reports*, **5**, 9892.
Ohler, M., Sanchez del Rio, M., Tuffanelli, A., Gambaccini, M., Taibi, A., Fantini, A. & Pareschi, G. (2000). *J. Appl. Cryst.* **30**, 1023.
Poulsen, H., Cook, P., Leemreize, H., Pedersen, A., Yildirim, C., Kutsal, M., Jakobsen, A., Trujillo, J., Ormstrup, J. & Detlefs, C. (2018). *J. Appl. Cryst.* **?**, ?–? Submitted.
Poulsen, H. F. (2012). *J. Appl. Cryst.* **45**, 1084–1097.
Poulsen, H. F. & Fu, X. (2003). *J. Appl. Crystall.* **36**, 1062–1068.
Poulsen, H. F., Jakobsen, A. C., Simons, H., Ahl, S. R., Cook, P. K. & Detlefs, C. (2017). *J. Appl. Cryst.* **50**, 1441–1456.
Ramar, A., Hata, S., Huang, X., Dunin-Borkowski, R. & Winther, G. (2010). *Risø International Symposium on Materials Science. Proceedings*, **31**, 397–404.
Schroer, C. G. & Lengeler, B. (2005). *Phys. Rev. Lett.* **94**, 054802.
Schuster, T. (2008). *Publications of the Scuola Normale Superiore*, **7**, 054802.
Simons, H., Ahl, S. R., Poulsen, H. F. & Detlefs, C. (2017). *J. Synchrotron Rad.* **24**(2), 392–401.
Simons, H., Haugen, A., Jakobsen, A., Schmidt, S., Stohr, F., Majkut, M., Detlefs, C., Daniels, J., Damjanovic, D. & Poulsen, H. (2018*a*). *Nature Mater.* **24**. In press.
Simons, H., Jakobsen, A. C., Ahl, S. R., Poulsen, H. F., Pantleon, W., Detlefs, C., Chu, Y.-H. & Valanoor, N. (2018*b*). *Nature Mater.* Submitted.
Simons, H., King, A., Ludwig, W., Detlefs, C., Pantleon, W., Schmidt, S., Stöhr, F., Snigireva, I., Snigirev, A. & Poulsen, H. (2015). *Nat. Commun.* **6**, 6098.
Snigirev, A., Kohn, V. G., Snigireva, I. & Lengeler, B. (1996). *Nature*, **384**, 49–51.
Tanner, B. K. (1976). *X-ray Diffraction Topography*. Oxford: Pergamon Press.

Ulvestad, A., Welland, M. J., Cha, W., Liu, Y., Kim, J. W., Harder, R., Maxey, E., Clark, J. N., Highland, M. J., You, H., Zapol, P., Hruszkewycz, S. O. & Stephenson, G. B. (2017). *Nature Mater.* **16**, 565–571.

Vaughan, G., Wright, J., Bytchkov, A., Rossat, M., Gleyzolle, H., Snigireva, I. & Snigireva, A. (2011). *J. Synchrotron Rad.* **18**, 125–133.

Williams, D. B. & Carter, C. B. (2009). *Transmission Electron Microscopy*. Springer, Berlin.